On the Characterization and Mitigation of Noise in Space-borne Microwave Sounding Instruments

Hu Yang*, *Member, IEEE,* Ninghai Sun, Edward Kim,Matthew Sammons, James Fuentes, James Kam, Xingming Liang, Cheng-Hsuan Lyu, Alexandra Bringer, Saji Abraham

***Abstract*—Space-borne microwave sounding instruments have become vital data sources for weather prediction and climate change studies. Among the various radiometer configurations, the total power microwave radiometer is particularly appealing for current and future operational satellites due to its superior sensitivity and simple design. However, its performance is vulnerable to degradation caused by receiver gain fluctuations, electronic 1/f noise, and other time varying receiver characteristics. For Numerical Weather Prediction (NWP) users, 1/f noise introduces inter-channel correlations, complicating the assimilation of affeced observations and reducing their accuracy. Addressing this noise issue in ground data processing system is essential to enhance the utility of microwave sounding data. This paper focuses on the characterization and mitigation of noise in current and future microwave sounding instruments, with particular emphasis on the impact of 1/f noise. Various methods are applied to quantitatively characterize noise features in both frequency and time domains. Additionally, the influence of calibration parameters on 1/f noise are analyzed. Based on these findings, we propose a mitigation algorithm for reducing noise during the on-orbit calibration of microwave sounding instruments, aiming to improve the quality of retrieved data for operational use.**

Microwave Sounder, striping noise, calibration

I. Introduction

Space-borne microwave sounding instruments are critical data sources for meteorological remote sensing applications. For current and future operational satellites, the total power radiometer is an appealing choice for its superior sensitivity and straightforward implementation compared to other radiometer configurations[1]. The Advanced Technology Microwave Sounder (ATMS) is a prominent example of a total power radiometer, first launched aboard the Suomi National Polar-orbiting Partnership (SNPP) satellite in 2011. As of this writing, two additional ATMS instruments are operational on NOAA-20 and NOAA-21 satellites. The ATMS features 22 channels distributed across five frequency bands: K (23.8GHz), Ka (31.4GHz), V (50.3 to ˜57.29 GHz), W (88.2GHz), and G (165.5GHz and 183 GHz) [2]. These instruments are considered part of the backbone of the global observing system, with three more ATMS sensors slated for future launches, including one aboard QuickSounder - a small satellite in NOAA's Near Earth Orbit Network (NEON) program [4]. Given this continued deployment, ATMS instruments are expected to remain a fundamental element of the observing system for decades. Despite their advantages, total power radiometer like ATMS are susceptible to performance degradation caused by receiver gain fluctuations, electronic 1/f noise, and other time varying receiver characteristics. Studies of SNPP ATMS data have revealed significant striping noise in observations, attribute to low-frequency 1/f noise within the instrument. This striping manifests as spatial patterns that impair data quality[3]. For NWP users, 1/f noise exacerbates inter-channel correlations, adversely affecting the assimilation of observations and leading to inaccuracies in weather models. Furthermore, as the development of next generation hyperspectral microwave sounding instruments advances, the noise performance remains a critical requirement for weather and climate applications. Addressing these noise issues is essential to maximize the utility of data from current and future microwave sounding instruments. Ground data processing systems must incorporate effective strategies to mitigate noise and enhance the quality of observations for operational use.

In nearly all areas of measurement, the ultimate limit of detecting weak signals is determined by noise. Some forms of noise are unavoidable, such as the real fluctuations in the quantity being measured, but they can be mitigated through the techniques like signal averaging and bandwidth narrowing. Other types, such as radio frequency interference and instrument electronic noise, can often be reduced or eliminated using filtering and low-noise design [5]. Noise is typically characterized by its frequency spectrum, amplitude distribution, and the physical mechanism responsible for its generation. In passive microwave sounding instruments, two primary noise types dominate: thermal noise (white noise) and 1/f noise (pink noise). Thermal noise exhibits a flat frequency spectrum, meaning its power remains constant across frequencies. It appears as random voltage variations and depends on factors such as the scene temperature, system equivalent noise temperature, bandwidth, and the integration time. Higher temperatures and resistances lead to greater noise amplitude. Statistically, thermal noise follows a Gaussian distribution with zero mean after normalization, and its effects can be significantly reduced through post-processing.

This study was supported by NOAA grant NA14NES4320003 (Cooperative Institute for Satellite Earth System Studies (CISESS) at the University of Maryland).
Hu Yang is with UMD/CISESS
Ninghai Sun is with ERT,
Edward Kim is with GSFC, NASA, Greenbelt, MD,
Matthew Sammons is with Fibertek Inc, GSFC, NASA, Greenbelt, MD,
James Fuentes and James Kam are with Northrop Grumman Space Systems, Azusa, CA,
XingMing Liang is with the Cooperative Institute of Earth System Studies, University of Maryland, supporting NOAA/NESDIS/STAR, College Park, MD 20740, USA,
Cheng-Hsuan Lyu is with Morgan State University, Maryland,
Saji Abraham is with SGT inc, GSFC, NASA, Greenbelt, MD,
Alexandra Bringer is with KBRwyle, GSFC, NASA, Greenbelt,MD

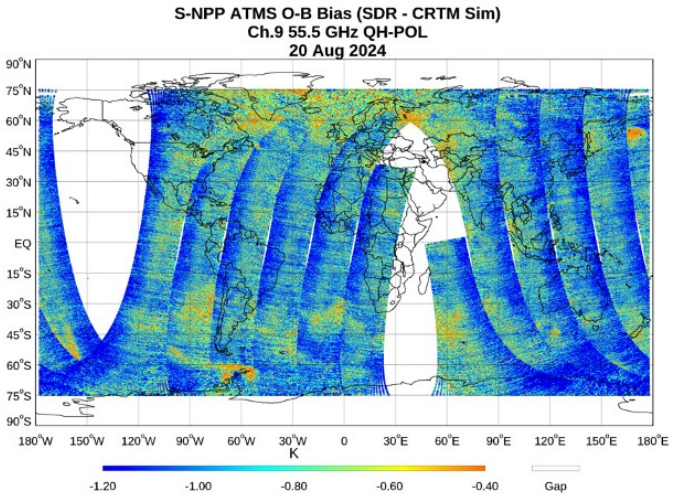

(a) On-orbit striping noise in channel 9 of SNPP ATMS

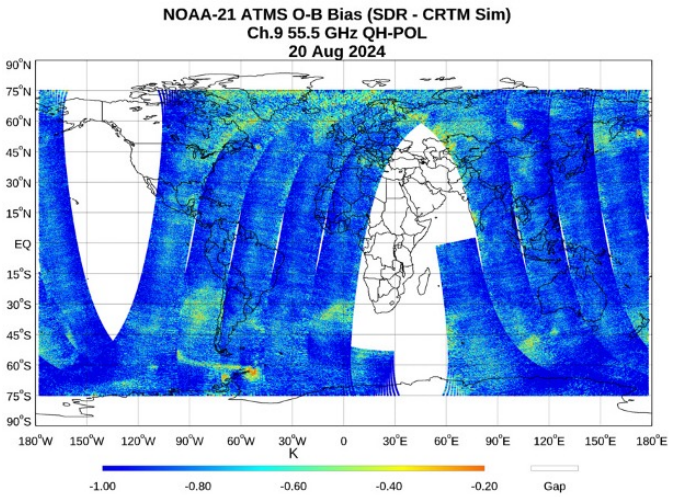

(b) On-orbit striping noise in channel 9 of NOAA-21 ATMS

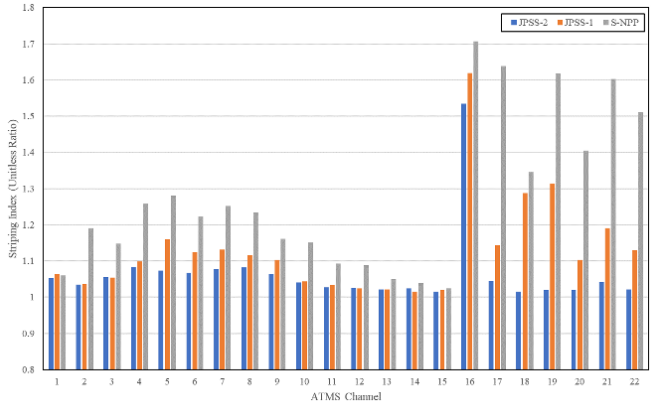

(c) Striping index comparison for all 22 channels between SNPP, NOAA-20 and NOAA-21 ATMS operational products

Fig. 1: Striping noise and the striping index in current operational ATMS units onboard the SNPP, NOAA-20 and NOAA-21 satellites

In contrast, 1/f noise follows a $1/f^{\alpha}$ power spectrum and manifests as low-frequency noise with a striped pattern in observations. Figure.1a illustrates the "O-B" results(observations minus radiative transfer model simulations) for the SNPP ATMS SDR product at channel 9, revealing visible striping patterns likely caused by instrument noise. For comparison, Figure 1b shows the same results for NOAA-21 ATMS, where striping is less pronounced. ATMS channel 9 has a weighting function that peaks at the top of troposphere, where atmospheric microwave radiation fluctuations are relatively steady. The striping observed in "O-B" thus originates from instrument noise. The striping index($\kappa_S I$) is used as a metric to quantify the significance of striping noise, defined as the ratio of variance in cross-track direction(σ^2_{CT}) to that in the along-track direction(σ^2_{AT}):

$$\kappa_{SI} = \frac{\sigma^2_{CT}}{\sigma^2_{AT}} \tag{1}$$

A value of $\kappa_{SI} = 1$ indicates no striping noise, while values greater than 1 signify increasing striping. Figure 1c compares striping index across SNPP , NOAA-20 and NOAA-21 ATMS instruments, showing significantly higher striping noise in SNPP data. However, the striping index measures relative significance rather than absolute magnitude. For NWP users, striping noise introduces channel correlation, adversely affecting data assimilation and reducing forecast accuracy[2].This makes striping noise a major concern for future applications, particularly for the NWP community. Unlike the white noise, which can be reduced by averaging consecutive samples, low-frequency striping noise requres more sophisticated approaches. Most striping mitigation algorithms, such as those combining Principal Component Analysis (PCA) and Ensemble Empirical Mode Decomposition (EEMD) have been tested on SNPP ATMS SDR data[6][7]. While effective for temperature sounding channels, these methods occasionally over-correct in W- and G-band channels, where non-uniform liquid water and cloud features are prominent. Additionally, processing large global datasets with these algorithms is time-intensive, presenting challenges for operational use. Moreover, current approaches lack mathmatical models to quantitatively evaluate spatial resolution degradation caused by low-pass filter-based mitigation.

This work addresses these challenges by investigating the impact of striping noise in ATMS measurements and proposing a new calibration algorithm to improve on-orbit calibration processes. Section II provides a detailed noise analysis of the SNPP ATMS, characterizing noise in both time and frequency domains. Section III examines the influence of calibration parameters on striping noise using datasets from ground thermal vacuum (TVAC) tests. Section IV details the development and evaluation of the new calibration algorithm. Additionally, Section V explores a dynamic window B-G algorithm as a post-processing step for total noise reduction. Conclusions and further discussions are provided in Section VI.

II. Noise Feature Characterization

To gain a deeper understanding of the noise characteristics in the original instrument measurements, data was collected

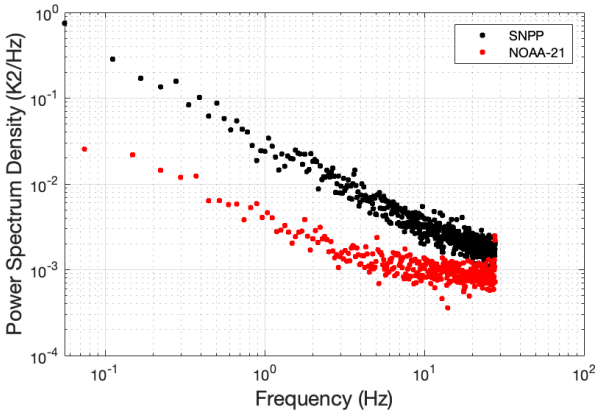

Fig. 2: Noise spectrum for SNPP and NOAA-21(JPSS-02) ATMS channel 16 (88.2GHz). Note that for SNPP, the noise power spectrum is modified with exaggerated 1/f noise to represent the worst case of the instrument noise performance

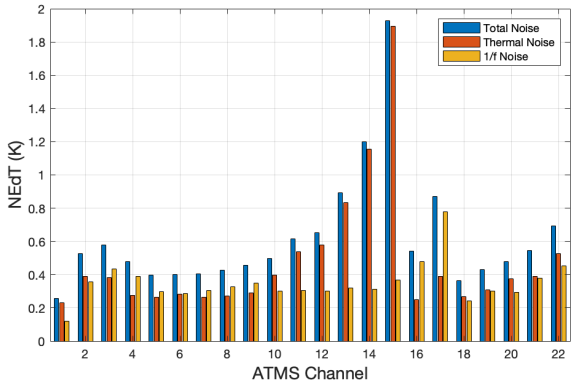

Fig. 3: Noise characterization for SNPP ATMS at scene temperature of 280K

from an external target with uniform and stable radiation. The calibrated noise data was then analyzed in both the frequency and time domains. For this study, the noise data was derived from the SNPP ATMS TVAC tests, with the $1/f$ noise component intentionally amplified to simulate a worst case scenario for future ATMS-like instruments.

A. Power Spectrum Analysis

The noise power spectral density (PSD) is commonly used as a metric to evaluate the frequency-dependent characteristic of the noise. To compute the PSD, the noise data in the time domain is first transformed into the frequency domain using a Fast Fouriier Transform (FFT). The PSD is then calculated using the following equation:

$$PSD(f) = \frac{1}{0.5 \cdot Fs \cdot N} \left\| FFT(t) \right\|^2 \tag{2}$$

Where $Fs = \frac{1}{0.018} = 55.6Hz$ is the sampling frequency of the instrument measurements, and N is number of data samples. The unit of the PSD is K^2/Hz. To minimize the noise in the results, the total number of 20,000 data samples (corresponding to 6 minutes continuous observations) were split into five segments, and the final PSD was obtained by averaging the PSD for each segment. Figure 2 presents the PSD calculation result for W-band (88.2GHz) of SNPP ATMS instrument, alongside a comparison with the NOAA-21 ATMS noise PSD.

As shown in Figure 2, the measured receiver power spectrum is the Root Sum Square (RSS) of two major components. At low frequencies, from DC to 10Hz, the PSD is inversely proportion to the frequency, reflecting the characteristics of $1/f$ noise. At frequencies above 10Hz, the spectrum transitions to a uniform Gaussian distribution with lower magnitude, representing white noise, whose PSD is indepdent of frequency. The frequency where the transition occurs is known as the 1/f corner frequency (FC), a critical performance: lower values indicate better performance. For NOAA-21 ATMS, the 1/f noise is significantly lower than for SNPP ATMS, as indicated by the lower corner frequency.

The PSD of the $1/f$ noise component can be modeled as an inverse function of the frequency:

$$PSD_{1/f}(f) = a \cdot f^{-\alpha} \tag{3}$$

Fitting results reveal that the PSD of SNPP ATMS increases steeply as frequency decreases. For instance, in the power spectrum shown in Figure 2, the value of alpha rises from 0.18 for NOAA-21 ATMS to 0.79 for SNPP ATMS, indicating a sharp increase in noise power at lower frequencies for the latter.

B. NEdT Analysis

The PSD analysis reveals two different noise components in the ATMS measurements: thermal (white) noise with uniform Gaussian spectrum and 1/f noise. Based on the method published in [8], the total noise in the measurements can be calculated using the following equation:

$$NEDT_{total} = \sqrt{\frac{1}{M-1} \sum_{i=1}^{M} \left(Tb^i_{noise} - \overline{Tb_{noise}} \right)^2} \tag{4}$$

The Noise equivalent differential Temperature (NEdT) for thermal noise can be determined from the two-elements Allan variance as:

$$NEDT_{thermal} = \sqrt{\frac{1}{2(M-1)} \sum_{i=1}^{M-1} \left(Tb^{i+1}_{noise} - Tb^i{}_{noise} \right)^2} \tag{5}$$

In these equations, Tb_{noise} represents the calibrated noise data samples in brightness temperature, M is the total number of noise data samples used in calculations. With the total noise and thermal noise determined, the 1/f noise can be calculated using:

$$NEDT_{1/f} = \sqrt{NEDT_{total}{}^2 - NEDT_{thermal}{}^2} \tag{6}$$

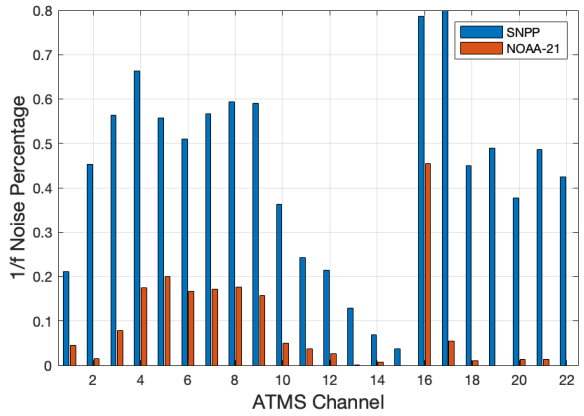

Fig. 4: Comparison of the 1/f noise percentages between SNPP and NOAA-21 ATMS

From Eq.4 to 6, the percentage contribution of $1/f$ noise can be calculated as the power ratio of $NEdT_{1/f}$ to $NEdT_{total}$ using the following equation:

$$\rho_{1/f} = \frac{NEDT_{1/f}^2}{NEDT_{total}^2} \tag{7}$$

The percentage of $1/f$ noise derived from Eq.7 serves as a metric for assessing the impact of $1/f$ noise in the measurements. As illustrated in Figure 4, for most of the V(50 60 GHz) and W (88.2GHz)-band channels, 1/f noise dominates the total noise in SNPP ATMS, contributing over 60%. In the G-band (165 183 GHz), while 1/f noise is lower, it remains a significant noise source.

It is noteworthy that the characteristics of $1/f$ noise depicted in Figure 4 align with the striping index shown in Figure 1c, highlighting a strong correlation between $1/f$ noise and the striping noise.

C. Channel Correlation Analysis

ATMS observations are a critical data source for NWP applications. Proper characterization of notable error correlations is essential for the effective assimilation of these observations. A Study of SNPP ATMS data at ECMWF indicates increased inter-channel correlations in ATMS compared to the legacy AMSU instrument, which is attributed to striping effects in the data[2]. The inter-channel error correlation coefficient can be calculated as below:

$$\begin{aligned}
\rho_{i,j} &= \frac{\mathrm{Cov}(X_i, X_j)}{\sigma_{X_i}\sigma_{X_j}} \\
\mathrm{Cov}(X_i, X_j) &= \frac{1}{m}\sum_{k=1}^{m}(X_i[k]-\mu_{X_i})(X_j[k]-\mu_{X_j}) \\
\mu_X &= \frac{1}{m}\sum_{k=1}^{m}X[k] \\
\sigma_X &= \sqrt{\frac{1}{m}\sum_{k=1}^{m}(X[k]-\mu_X)^2}
\end{aligned} \tag{8}$$

Where X_i and X_j represent the noise data for channels i and j, respectively, and m is the number of data samples for each channel.

Figure 5 illustrates the inter-channel error correlation for SNPP and NOAA-21 ATMS, derived from the same noise data samples used for the PSD and NEdT analyses. The results reveal a significant increase in inter-channel correlations for the V- and G-band channels in SNPP ATMS.

The analysis of ATMS noise data shows that the high percentage of $1/f$ noise in the noise signal strongly contributes to increased inter-channel error correlations. This underscores the importance of mitigating $1/f$ noise to reduce such correlations and improve the quality of ATMS observations for NWP applications.

III. Impacts of Calibration Parameters on the Striping Noise

The Study by Hersman and Poe demonstrates that the noise performance of a total power radiometer with periodic absolute calibration, such as ATMS, is fundamentally linked to the receiver output noise power spectrum, $S_r(f)$, and the calibration processor transfer function $H(f)$, as described by the following equation [9]:

$$(\Delta T)^2 = c^2 \int_0^\infty df S_r(f) H(f) \tag{9}$$

The transfer function $H(f)$ depends on the radiometer parameters, including the observation integration time τ, calibration duration tc, and the weighting function applied to calibration samples. as shown in [9], both integration time and calibration duration significantly affect the noise characteristic of the calibrated brightness temperature.

This section explores the influence of calibration parameters on the noise characteristics of the calibrated brightness temperature for ATMS. Specifically, the effects of calibration duration, receiver integration time, and the weighting function applied to calibration data are analyzed.

A. Impacts of the Weighting Function

As described in [9], the power spectrum of the calibration transfer function $H(f)$ can be expressed as a function of the integration time for scene observation τ_s, integration time for calibration samples τ_c, calibration time tc, and the weighting function for the calibration samples:

$$H(f) = \left|\frac{sin(\pi f \tau_s)}{\pi f \tau_s} - \frac{sin(\pi f \tau_c)}{\pi f \tau_c}\sum_k w(t_s - k t_c) e^{-j2\pi f(t_s - k t_c)}\right|^2 \tag{10}$$

for ATMS instruments, $\tau_s = \tau_c = 0.018s$. During on-orbit calibration, four consecutive calibration samples from the cold space and warm load are averaged, resulting in an effective $\overline{\tau_c} = 4\tau_c$. Typically, a boxcar weighting function with varying window size is used for different channel in the calibration process.

To assess the impact of the weighting function's window size on the calibration process, $H(f)$ was generated for the calibration times of 2.67s, 13.35s, and 26.7s, corresponding to window sizes of 1, 5, and 10 scan lines, respectively. As

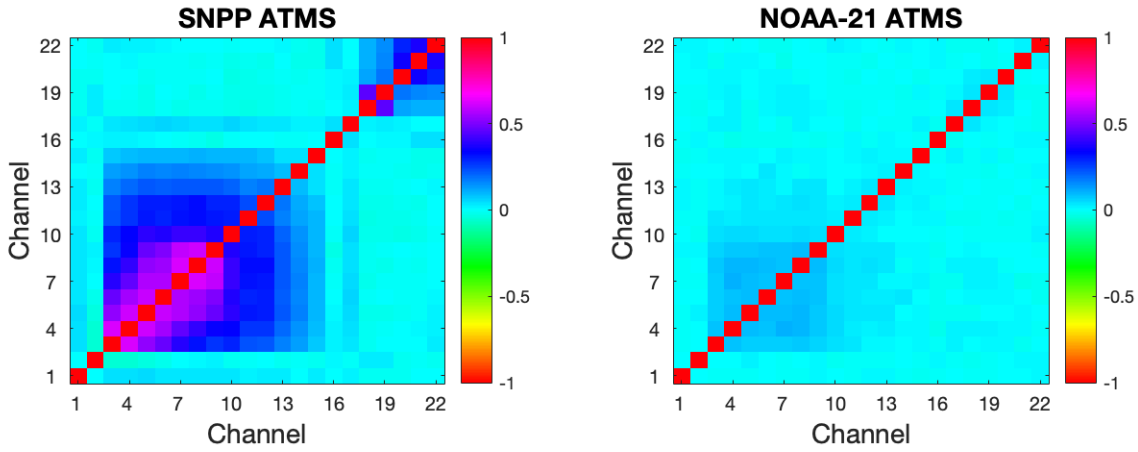

Fig. 5: Comparison of the inter-channel error correlations between SNPP and NOAA-21 ATMS

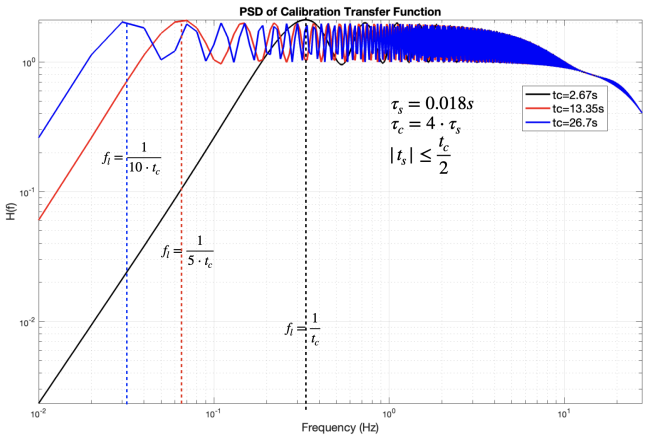

Fig. 6: Impacts of window size of the weighting function on calibration process function

shown in Figure 6, the calibration transfer function acts as a band-pass filter for the signal's PSD. It attenuates signals with frequencies lower than the calibration frequency ($f_l = 1/t_c$) and allows signal between f_l and the sampling frequency $f_h = \frac{1}{2\tau_s}$ to pass. With an increasing window size, the stop frequency f_l shifts to the lower end of the frequency spectrum, incorporating more low-frequency $1/f$ noise into the calibration results.

Additionally, a boxcar weighting function with window size ranging from 1 to 50 was also applied to the calibration data collected from a constant scene temperature of 280K, the total noise and $1/f$ noise were calculated to evaluate the weighting function's impact on calibration noise. As shown in Figure 7, for SNPP ATMS K-(23.8 GHz), Ka-(31.4GHz) and V-band (50 60GHz), both total noise and $1/f$ noise decrease with the increase of the window size and stabilized at window size of 10. In contrast, for W-(88.2GHz) and G-(165 183GHz) band, increasing the window size reduces total noise but increases $1/f$ noise.

B. Impacts of calibration time

To investigate the impact of calibration time on the noise feature of calibrated observations, original continuous observations were calibrated with different calibration times of t_s,$5t_s$,$10t_s$, and $50t_s$, with $t_s = 18ms$. PSD analysis was then performed on the calibrated noise data for different calibration times to assess the impact of the calibration time on $1/f$ rejection. Figure 8 shows the PSD calculation results for ATMS channel 8, indicating that the 1/f noise increased sharply with increasing calibration time.

C. Impacts of the integration time

To investigate the impact of integration time on the $1/f$ noise in the calibrated observations, the same dataset was used with a constant calibration time of 8/3 seconds and a sampling time of 0.018 seconds. The percentage of 1/f noise was then calculated by using Eq.7. As shown in Figure 9, the percentage of 1/f noise increases as the integration time increases up to around 200ms, due to the sharp decrease of the thermal noise. However, as the integration time is further increased, the percentage of $1/f$ noise decreases due to reduced 1/f noise.

IV. Calibration Algorithm for Striping Mitigation

From section III, it is evident that for microwave observations with significant $1/f$ noise, data quality can be enhanced by reducing the calibration time and increasing the integration time. Additionally, an appropriate selection of the weighting function window size for calibration data can further mitigate $1/f$ noise in the calibrated products. For operational satellite observations, traditional calibration algorithms typically rely on a two-point calibration approach, applying a fixed window to calibration samples to reduce noise.

In this paper, we propose a novel calibration algorithm based on a differential calibration scheme. Unlike traditional methods that calibrate at a fixed calibration time T_c, this approach calibrates the calibration gain at each scene observation time t_s. The scene temperature is then derived by taking the differential of the receiver output counts.

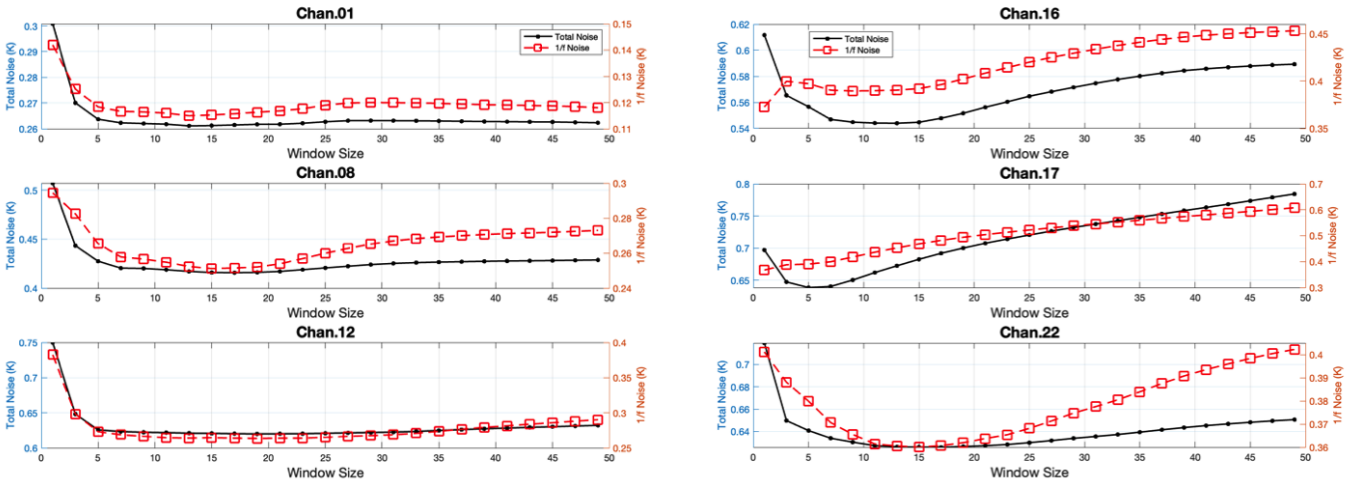

Fig. 7: Impacts of weighting function window size on the calibration noise. The results are calculated based on the modified SNPP noise measurements

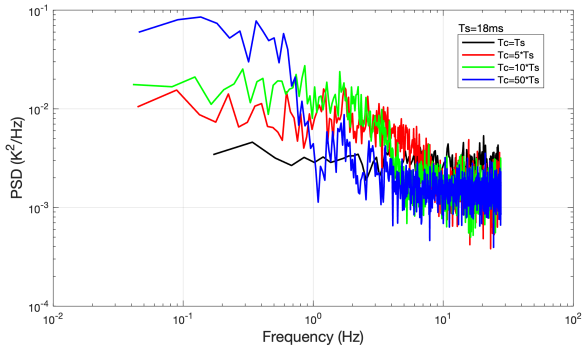

Fig. 8: Noise power spectrum for the calibrated noise measurements in ATMS channel 8 with different calibration time of t_s,$5t_s$,$10t_s$, and $50t_s$

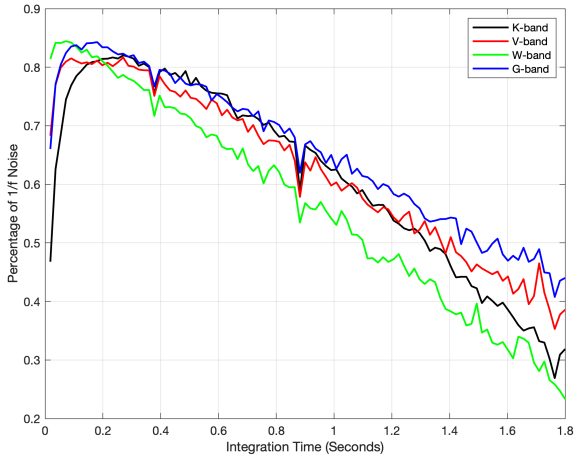

Fig. 9: Percentage of 1/f noise for the calibrated noise measurements in different detection bands of ATMS with integration time varies from 0.018 to 1.8 seconds

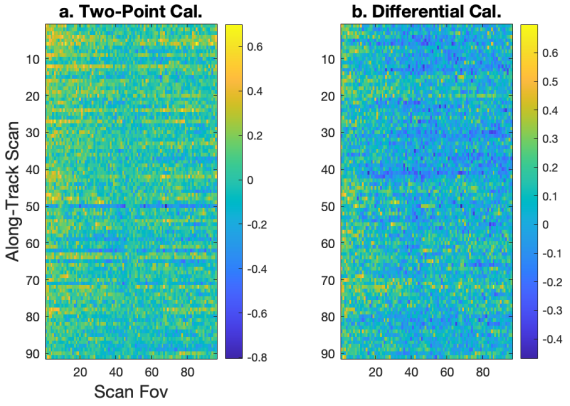

Fig. 10: Comparison of the noise calibration results between the traditional two-point calibration (a) and the new differential calibration (b). Presented is the deep space scan observations for SNPP ATMS channel 8

A. *Differential Calibration Algorithm*

As demonstrated in section II, the two-element Allan variance can effectively assess thermal noise within the noise signal. For noise signals containing non-Gaussian noise components, these components can be transformed into Gaussian noise. Additionally, section III shows that shortening the calibration time can enhance the $1/f$ noise rejection, thereby reducing its impact. Building on these analyses, we propose the following new calibration algorithm for on-orbit satellite calibration:

$$\begin{aligned} Ta_{i+1} &= Ta_i + \widehat{G}_i[CS(i+1)) - CS(i)], i = 1, N \\ Ta_1 &= \widehat{G}_i(i=1) \cdot (CS_1 - \widehat{CW}_i(i=1)) + \widehat{Tw}_i(i=1) \end{aligned} \tag{11}$$

Here,

- Ta_i is the calibrated temperature for the ith scene observation sample,

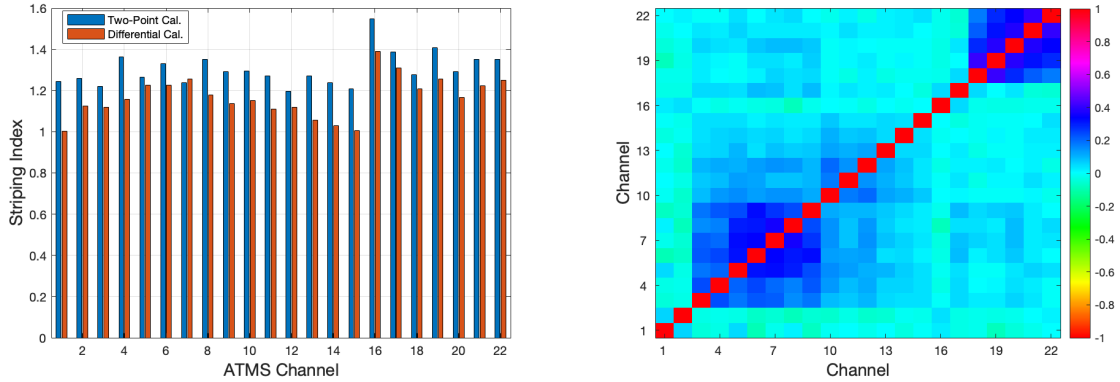

Fig. 11: Evaluation results of the striping index and channel correlation for the new calibration algorithm

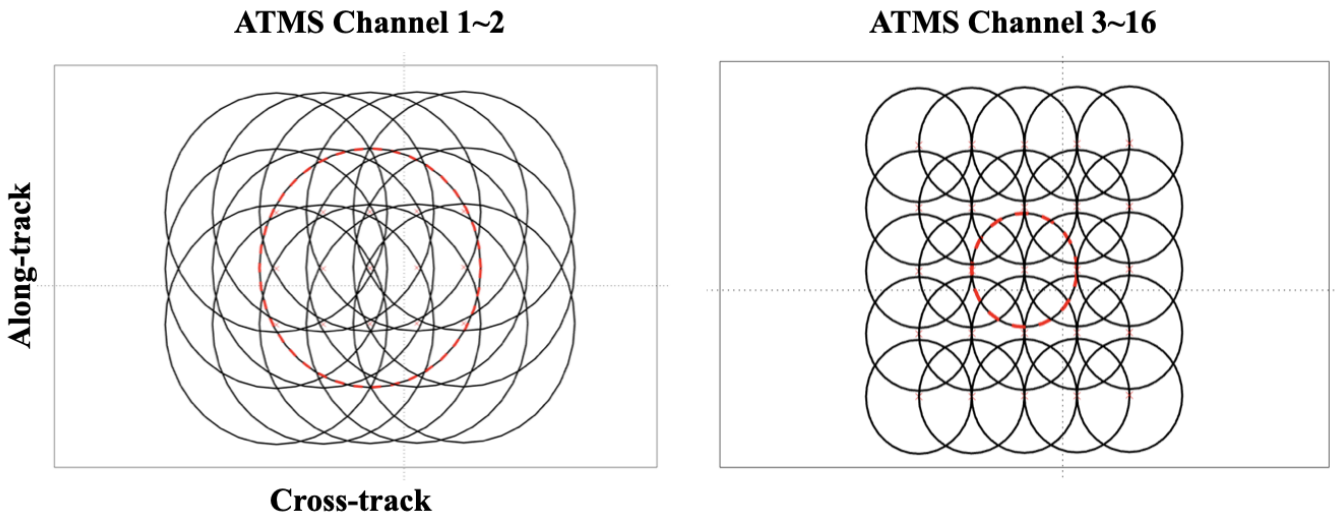

Fig. 12: ATMS Earth Scene Scan Geometry in K/Ka(left) and V/W band (right). Each circle is 3dB contour Instantaneous Field of View (IFOV) at center of a Beam Position (BP) at nadir

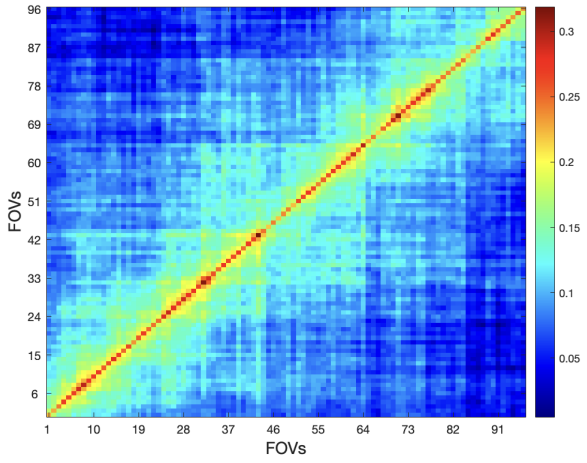

Fig. 13: SNPP ATMS channel 16 noise error covariance matrix

- CS_i denotes the corresponding receiver output counts,
- $\widehat{Tw}$ and $\widehat{CW}$ are the brightness temperature and receiver outputs for the calibration reference at each of the observation time ts, and
- $\widehat{G}$ is the calibration gain calculated at ts.

B. Application and Validation of the New Calibration Algorithm

To evaluate the impacts of the new calibration method on noise characteristics in the calibrated results, special datasets from the SNPP pitch maneuver observations were utilized in this study. On February 20, 2012, the Suomi NPP satellite, equipped with an ATMS, executed a pitch maneuver to scan deep space, collecting 18-minutes of data across 96 fields of view (FOVs) per scan. In principle, the brightness temperatures calibrated from the cold space should exhibit uniformity across the scan.

Figure 10a illustrates the calibrated brightness temperatures using the traditional two-point calibration approach, where the original receiver output counts were calibrated at a fixed calibration time t_c every 2.67s. In contrast, Figure 10b presents the

results from the new calibration algorithm based on Eq.(11), in which the original counts were calibrated at the observations time t_s every 0.018s. During the calibration process, the scan-angle-dependent antenna emission was corrected using a physical model developed in previous study[12].

The results demonstrate that the new calibration algorithm effectively reduces the striping pattern in the calibrated brightness temperatures. To quantify this improvement, the striping index and channel correlation were calculated, with the results shown in Figure 11. Using the differential calibration algorithm, the striping noise was reduced by an average of 12% for K/Ka and V bands, and 10% for W and G bands.

V. Dynamic Window B-G algorithm

When white noise dominants the noise signal, as is the case for most of the current operational microwave sounding instruments, the total noise remains largely unaffected by the new calibration algorithm. To further reduce the total noise in the calibrated brightness temperature, a dynamic window-based B-G algorithm has been developed and applied. This approach leverages the oversampling capability inherent in the ATMS instrument's scanning geometry.

As illustrated in Figure 12, ATMS scanning geometry includes overlapping observations. By exploiting the redundant information from the consecutive FOVs, a mathematical model can be constructed to account for both the degradation in spatial resolution and the reduction in the noise. This model enables the derivation of a set of weighting coefficients to generate new observations within predefined FOV sizes from the overlapping original observations, simultaneously reducing noise to the desired level.

A. The Math Model

For a space-borne microwave radiometer with a scanning antenna, Earth observations can be modeled as the convolution of the noisy scene brightness temperature with the antenna gain function G as below:

$$Ta(\rho_0) = \int Tb(\rho) G(\rho_0, \rho) \tag{12}$$

Here, $Tb(\rho) =$ represents the scene brightness temperature at location ρ, and $G(\rho_0, \rho)$ is the normalized antenna gain centered at ρ_0.

For instruments with oversampling design, new observations at the desired spatial resolution can be reconstructed from overlapping footprints of the original observations:

$$Ta_{new}(\rho_0) = \sum_{i=1}^{n} a_i \cdot Ta_{org}(\rho_i) \tag{13}$$

In this equation, Ta_{org} denotes the original antenna observations, expressed as the sum of the scene brightness temperature and instrument noise:

$$Ta_{org}(\rho_0) = \int [Tb(\rho_i) + \Delta T_{noise}(\rho_i)] G(\rho_0, \rho_i) dA \tag{14}$$

The noise in the new observations is derived from the noise variance of the original observations:

$$\Delta T^2_{noise} = \widehat{\sigma} = a^T E a \tag{15}$$

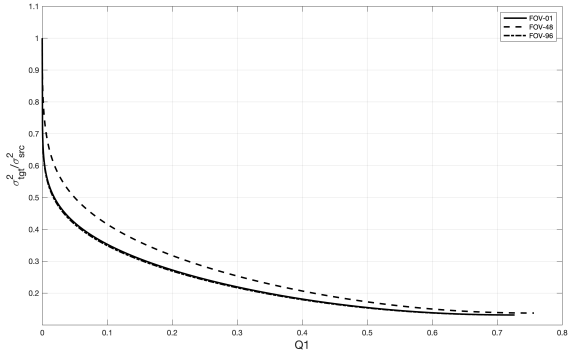

Fig. 14: Trade-off curve for reduction of noise and degradation of spatial resolution for ATMS 2.2°beam width channels

Here, a represents the weighting coefficients, and E is the error covariance matrix of the original measurements, calculated from the instrument noise observations for each channel. Figure 13 presents the error covariance matrix for SNPP channel 16. Since each channel exhibits distinct noise characteristics, the covariance matrix must be calculated separately for each channel.

For operational applications, such as numerical weather prediction(NWP), the goal is to reduce noise to acceptable levels without significantly degrading spatial resolution of the original observations. To achieve this, a set of optimal weighting coefficients (a_i) is derived by minimizing the following objective function Q [10]:

$$Q = Q_0 \cos\gamma + \widehat{\sigma} w \sin\gamma \tag{16}$$

The first term in Eq.(16) measures the spatial resolution loss by evaluating the difference between the new and target antenna patterns:

$$Q_0 = \int \left[\sum_{i=1}^{n} \sum_{j=1}^{n} a_{ij} G_{ij}(\widehat{\rho}) - F(\widehat{\rho}_0, \widehat{\rho}) \right]^2 dA \tag{17}$$

Here, G_{ij} represents the antenna gain for the original observations at position (i,j) , and$F$ is the target antenna pattern for the new observation at ρ_0.

The second term in Eq.(16) represents the noise in the new observations, with $\widehat{\sigma}$ calculated from Eq.15. The parameter γ, ranging from 0 to $\pi/2$, adjusts the trade-off between spatial resolution and noise reduction. At $\gamma = 0$, spatial resolution is preserved, while increasing γ prioritizes noise reduction at the cost of spatial resolution.

The optimal coefficients $a_{i,j}$ can be determined using the following expression [10][11]:

$$a = S^{-1} \left[\cos\gamma \cdot v + \frac{1 - \cos\gamma \cdot u^T S^{-1} v}{u^T S^{-1} u} \cdot u \right] \tag{18}$$

Here, S is the covariance matrix of the measurements, u is a vector of original antenna weights, and v represents the correlation between the original antenna gain and the target antenna gain for the observations. For operational applications,

the optimal value for γ needs to be determined for channels with different footprint size at the different scan positions.

B. Calculation of the Remapping Weighting Coefficients

For the ATMS noise mitigation algorithm, the primary challenge is to reduce the noise to the same level as the current operational ATMS unit without significant degrading spatial resolution. To achieve this, an antenna pattern identical to the original antenna beam is selected as the target antenna pattern in Eq.17, such that $F(\widehat{\rho}_0, \widehat{\rho}) = G(\widehat{\rho}_0, \widehat{\rho})$. Based on our previous study in [13],a dynamic window technique is employed to derive the coefficients a in Eq.17. Figure 14 shows the trade-off curves between noise reduction and the spatial resolution degradation for channels with an original beam width of 2.2 °. To generate these curves, the parameter γ is varied from 0 to the maximum value of $\pi/2$ in steps of 0.01. For each γ, a set of coefficients a is calculated from Eq.18. Using these coefficients, the ratio of the new noise to the original noise is determined from Eq.13. The loss of spatial resolution is then computed using the normalized Q_0 in Eq.17 as follow:

$$\widehat{Q} = \frac{Q_0}{\iint G(\widehat{\rho}_0, \widehat{\rho}) dA} \tag{19}$$

Figure 14 reveals that noise reduction is accompanied by spatial resolution degradation. For instance, reducing noise by 50% results in a 5% degradation in spatial resolution. Futher reducing the noise to 20% of the original level leads to a 50% degradation in spatial resolution. It is also worth noting that the trade-off curve varies slightly with scan positions. For scan positions closer to the nadir view (e.g., FOV-48), spatial resolution degradation is more sensitive to changes in noise.

C. Evaluation of the Noise Mitigation Algorithm

In this study, γ is determined based on the preset noise ratio, defined as $NR = \frac{\sigma^2_{tgt}}{\sigma^2_{src}}$. The trade-off between noise and spatial resolution in ATMS channels requires different considerations depending on the channel type. For window channels, placing greater emphasis on the $\widehat{Q}$ terms can help minimize the impact of noise mitigation. In contrast, for sounding channels in V and G bands, the noise term requires higher weighting since noise reduction is more critical for applications such as NWP and climate studies.

To address this, two noise ratios, $NR = 0.5$ and $NR = 0.2$, were selected to generate the weighting coefficients. A comprehensive evaluation of the changes in spatial resolution and noise characteristics in the new dataset is essential for the user community. This paper evaluates these changes using model-simulated datasets. Specifically, simulated ATMS observations for Hurricane Sandy at 0600 UTC October 28, 2012, were generated using the Community Radiative Transfer Model (CRTM) with inputs from a $3 \times 3Km$ grid of a 66-hours forecast from the Hurricane Weather Research and Forecasting model (HWRF) model. Details of the simulation process provided in [11]. To ensure the simulated datasets exhibit the same noise characteristics as the operational instrument observations, the noise spectrum datasets in Section II were utilized to generate noise brightness temperatures, which were added to the simulated antenna temperature for ATMS observations. For reference, the antenna temperature of NOAA-21 was also simulated using the noise spectrum derived from the ground tests.

TABLE I: Comparison of the Footprint Size between the Original and New Observations for $\frac{\sigma_{new}}{\sigma_{old}} = 0.5$ and $\frac{\sigma_{new}}{\sigma_{old}} = 0.2$

Scan Position	X^{Org}_{3dB} (Km)	Y^{Org}_{3dB} (Km)	ΔX (NR=0.5)	ΔY (NR=0.5)	ΔX (NR=0.2)	ΔY (NR=0.2)
1	142.4	70.7	3.3	8.3	36.6	36.1
48	33.2	31.9	8.5	7.3	26.5	21.3
96	144.7	61.7	5.3	9.8	43.3	37.2

In this study, SNPP ATMS channel 16 was selected to evaluate the noise mitigation algorithm due to its significant $1/f$ noise and highly non-homogeneous scene, making it a worst case scenario for the implementation. Figure 15 presents the noise mitigation results, showing a substantial reduction in the striping features in the new observations compared to the original data.

Additionally, the changes in spatial resolution and noise characteristics in the observations were evaluated to assess the effectiveness of the noise mitigation algorithm.

1) Evaluation of the Changes in Spatial Resolution: The change in spatial resolution at different scan positions was assessed by comparing the 3dB footprint size between the original and the new observations. Figure 16 illustrates the 3dB footprints at scan position 1, 48 and 96 for both the original and new observations. A two-dimension Gaussian function was used to model the antenna patterns projected onto the Earth surface with a grid resolution of $3 \times 3Km$:

$$G(x, y) = Aexp(-(\frac{x - x_0}{2\sigma^2_x} + \frac{y - y_0}{2\sigma^2_y})) \tag{20}$$

The 3dB footprint size was derived as the Full Width at Half Maximum (FWHM) using the following equations:

$$\begin{aligned} FWHM_X &= 2\sqrt{2ln(2)} \cdot \sigma_x \\ FWHM_Y &= 2\sqrt{2ln(2)} \cdot \sigma_y \end{aligned} \tag{21}$$

Table 1 presents the footprint sizes for the original observations and the changes observed in the new measurements at scan positions 1, 48, and 96, with units in kilometers. For a noise reduction factor (NR) of 0.5, the footprint size increases by an average of 8 km at the scan center and 5 km at the scan edges. However, for NR=0.2, the spatial resolution degradation becomes more pronounced, with an increase of 23 km at the scan center and 36 km at the scan edges.

2) The Total Noise: The total noise for the noise mitigation results at NR=0.5 and NR=0.2 was calculated using the equation provided in section II. As shown in figure 17, the total noise was reduced to approximately 50% and 20% of the noise levels in the original observations, respectively. For the NR=0.5 results, the noise in the low V-band of the new observations is comparable to that of NOAA-21 ATMS, while the the high V-band demonstrates improved performance.

3) $1/f$ noise: To assess changes in $1/f$ noise in the noise reduction products, PSD analysis was conducted on both the original and new observations. Figure 18 presents the PSD

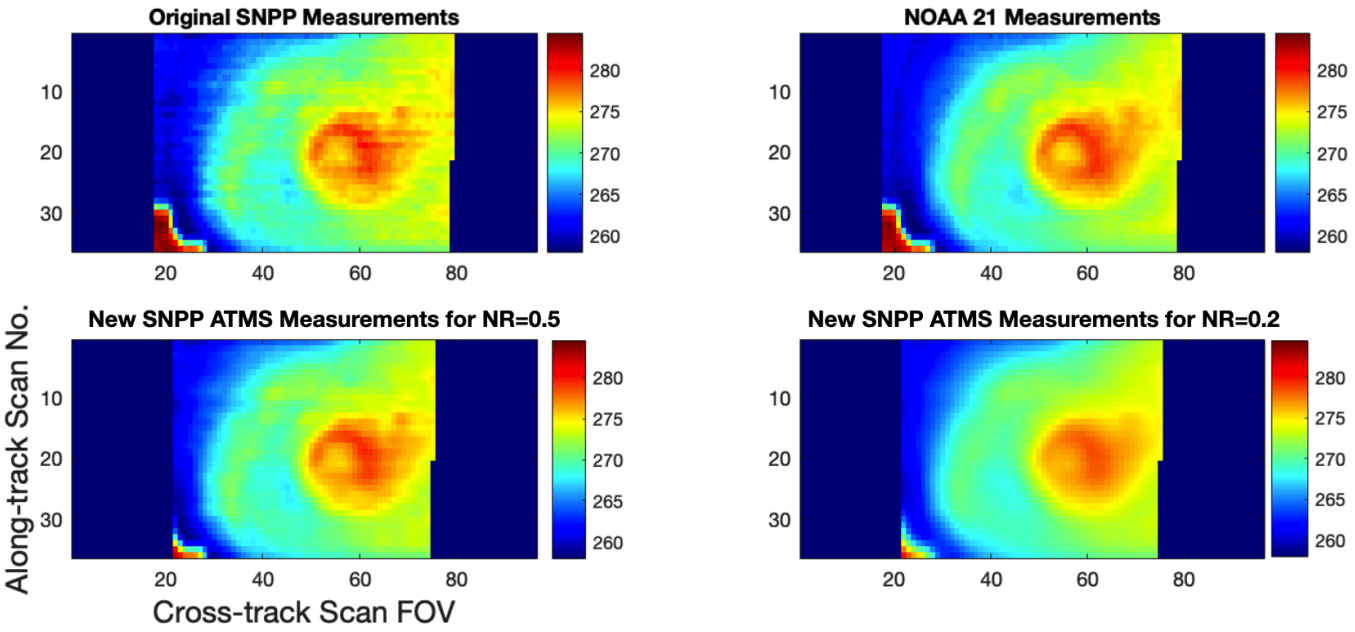

Fig. 15: Results for implementation of the noise mitigation algorithm on SNPP ATMS channel 16. The top panels are the simulated original SNPP and NOAA 21 ATMS observations; the bottom panels are the noise mitigation results for NR=0.5 and NR=0.2. The color bar is in kelvins

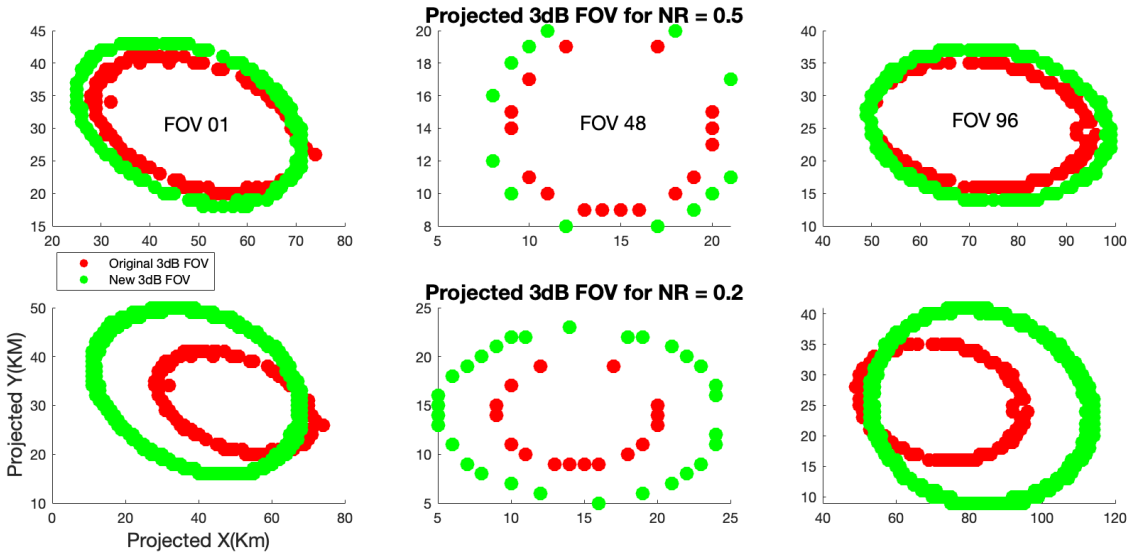

Fig. 16: Comparison of the footprint size between the original and new observations

analysis results for ATMS channel 16, corresponding to noise ratio of 0.5 and 0.2. For reference, the PSD of the original SNPP and NOAA-21 ATMS data was also calculated.

As shown in the figure, for NR=0.5, the magnitude of white noise component at frequency above 10Hz is significantly reduced after applying the noise mitigation algorithm. For NR=0.2, both $1/f$ noise and white noise are attenuated, but to different extents. To quantify the change in $1/f$ noise, the following metric is used:

$$R_{1/f} = \frac{\int_0^{f_C} PSD(f)df}{\int_0^{f_H} PSD(f)df} \tag{22}$$

Here, $f_C = 10Hz$ represents the corner frequency that separates the $1/f$ noise from white noise, $f_H = 0.5 \cdot Fs$ is the maximum frequency in the noise signal, equal to half the sampling frequency Fs. $PSD(f)$ denotes the noise power spectrum density for the original observations. The $1/f$ noise ratio at NR=0.5 and NR=0.2 was calculated for ATMS channel 3 to 16, and results shown in figure 19. The figure reveals

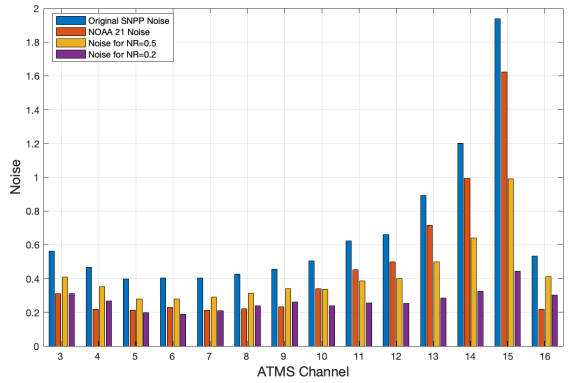

Fig. 17: NEdT evaluation results for implementation of the noise mitigation algorithm on SNPP ATMS channels 3 to 16. Results for both NR=0.5 and NR=0.2 are included

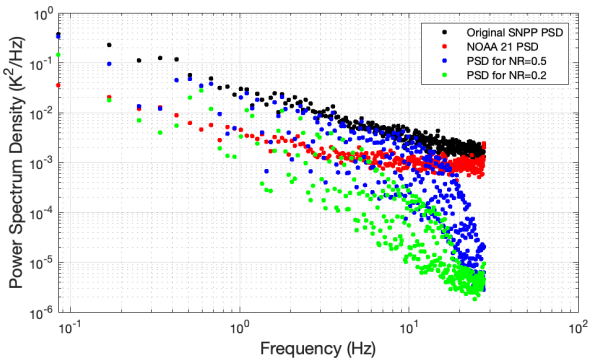

Fig. 18: Power spectrum evaluation results for the noise mitigation results at ATMS channels 16. Results for both NR=0.5 and NR=0.2 are included

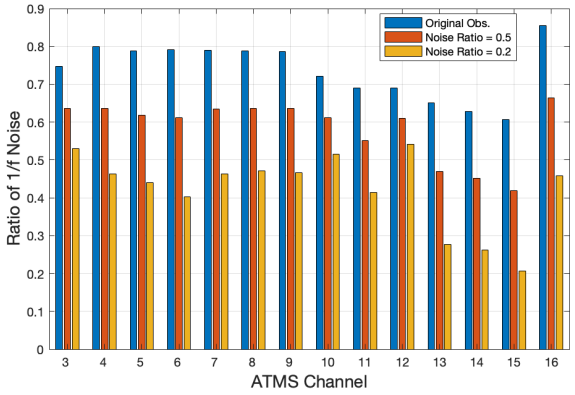

Fig. 19: The Noise ratio between the 1/f portion and the total PSD. Results for original observations (blue bar) and new observations at NR=0.5 (red bar) and NR=0.2 (yellow bar) in ATMS channel 3 to 16 are presented

that the reduction in $1/f$ noise varies across channels. For channel 16, the original $1/f$ noise constituted 85% of the total noise in the initial measurement. After applying the noise mitigation algorithm, the proportion decreased to 65% percent for $NR = 0.5$ and 45% for $NR = 0.2$.

4) Channel Correlation: As discussed in section III, the inter-channel correlation is primarily influenced by the percentage of $1/f$ noise in the total noise signal, rather than its absolute magnitude. Evaluation results demonstrate that the dynamic window B-G noise mitigation algorithm effectove;u reduces both the magnitude of $1/f$ noise and white noise compared to the original measurements. However, the corrected noise power remains inversely proportional to the frequency, as illustrated in Figure 18.

Figure 20 represents the inter-channel noise error correlation for ATMS V-band channels 3 to 15 in the new datasets with NR=0.5 and NR=0.2, derived from the simulated noise signal. The results indicate that as the percentage of $1/f$ noise in the total noise increases after applying the noise mitigation algorithm, there is corresponding rise in inter-channel correlation.

VI. Summary and Conclusions

The presence of Significant striping noise in measurements degrades the quality of calibrated radiance products and negatively impacts on various applications. This paper investigates the effects of striping noise and explores a new method to mitigate it during the calibration process. Preliminary results indicate that enhancing the calibration performance for 1/f noise rejection effectively reduces striping noise in calibrated measurements.

Additionally, applying a noise mitigation algorithm based on the dynamic-window B-G method further reduces total noise to the required level. It is also observed that when white noise dominates the measurements, the proposed method effectively minimizes noise without significantly compromising spatial resolution.

The proposed algorithm can be seamlessly integrated into the operational calibration process with minimal computational overhead. Future work will focus on testing the method for broader operational applications.

References

[1] Niels Skou and David Le Vine, “Microwave Radiometer Systems, Design and Analysis”, second edition, Artech House, 2006.

[2] E. Kim et al., “An Evaluation of NOAA-20 ATMS Instrument Pre-Launch and On-Orbit Performance Characterization”, in IEEE Transactions on Geoscience and Remote Sensing, vol. 60, pp. 1-13, 2022, Art no. 5302813, doi: 10.1109/TGRS.2022.3148663.

[3] Niels Bormann, Anne Fouilloux, William Bell, “Evaluation and assimilation of ATMS data in the ECMWF system”, JOURNAL OF GEOPHYSICAL RESEARCH: ATMOSPHERES, VOL. 118, 12,970–12,980, doi:10.1002/2013JD020325, 2013.

[4] “Near Earth Orbit Network (NEON)”, https://www.nesdis.noaa.gov/our-satellites/future-programs/near-earth-orbit-network-neon.

[5] Paul Horowitz, Winfield Hill, “The Art of Electronics”, Third Edition, Cambridge, 2015.

[6] Xiaoxu Tian and Xiaolei Zou, 2019, “Mitigation of Striping Noise in ATMS Calibration Counts by Symmetric Filters”, Journal of Atmospheric and Oceanic Technology, Vol.36, No.7, pp.1297-1312.

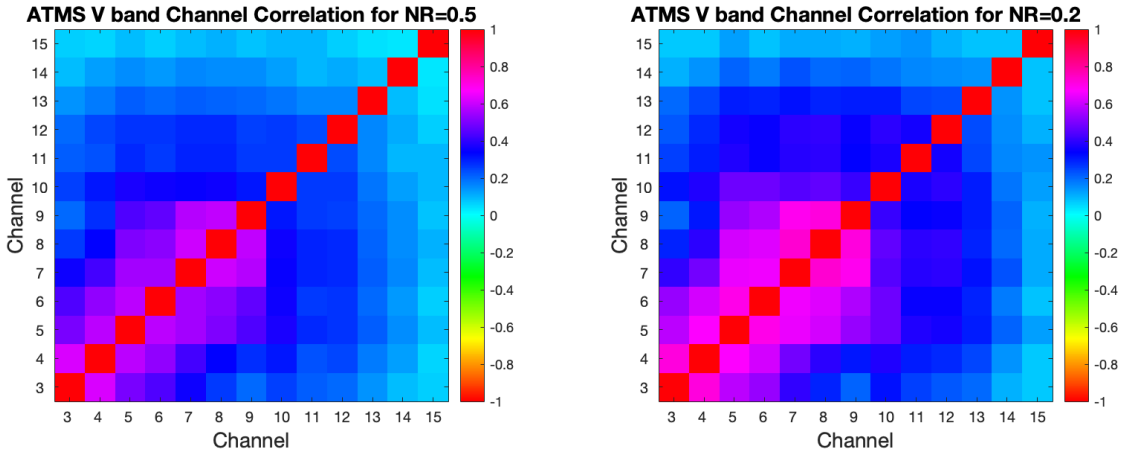

Fig. 20: channel error correlation for the noise mitigation results at ATMS V band channels 3 to 15. Left is for NR=0.5 and right is for NR=0.2

[7] Zou, X., Dong, H. and Qin, Z. (2017), "Striping noise reduction for ATMS window channels using a modified destriping algorithm", Q.J.R. Meteorol. Soc, 143: 2567-2577. https://doi.org/10.1002/qj.3107.

[8] J. X. Yang and H. Yang, "A New Algorithm for Determining the Noise Equivalent Delta Temperature of In-Orbit Microwave Radiometers", in IEEE Transactions on Geoscience and Remote Sensing, vol. 60, pp. 1-11, 2022, Art no. 5301611, doi: 10.1109/TGRS.2021.3097594.

[9] Michael Hersman and Gene Poe, "Sensitivity of the Total Power Radiometer with Periodic Absolute Calibration", IEEE TRANSACTIONS ON MICROWAVE THEORY AND TECHNIQUES, VOL. MTr-29, NO. 1, pp.33-40, JANUARY 1981.

[10] A. Stogryn, "Estimates of Brightness Temperatures from Scanning Radiometer Data", IEEE Transaction on antennas and Propagation,Vol.AP-26,No.5, PP. 720-726, 1978

[11] H. Yang and X. Zou, "Optimal ATMS Remapping Algorithm for Climate Research", in IEEE Transactions on Geoscience and Remote Sensing, vol. 52, no. 11, pp. 7290-7296, Nov. 2014, doi: 10.1109/TGRS.2014.2310702.

[12] H. Yang, F. Weng and K. Anderson, *"Estimation of ATMS Antenna Emission From Cold Space Observations"*, IEEE Transactions on Geoscience and Remote Sensing, vol. 54, no. 8, pp. 4479-4487, Aug. 2016, doi: 10.1109/TGRS.2016.2542526.

[13] J. Zhou, H. Yang and R. Iacovazzi, "Improving ATMS Remapping Accuracy Using Adaptive Window and Noise-Tuning Method in Backus–Gilbert Inversion", in IEEE Transactions on Geoscience and Remote Sensing, vol. 60, pp. 1-12, 2022, Art. no. 5304412, doi: 10.1109/TGRS.2022.3182630.